How Mn/Ni Ordering Controls Electrochemical Performance in High-Voltage Spinel $LiNi_{0.44}Mn_{1.56}O_4$ with Fixed Oxygen Content

Aktekin, Burak; Massel, Felix; Ahmadi, Majid; Valvo, Mario; Hahlin, Maria; Zipprich, Wolfgang; Marzano, Fernanda; Duda, Laurent; Younesi, Reza; More Authors

DOI
10.1021/acsaem.0c01075

Publication date
2020

Document Version
Final published version

Published in
ACS Applied Energy Materials

ACS APPLIED ENERGY MATERIALS

www.acsaem.org Article

How Mn/Ni Ordering Controls Electrochemical Performance in High-Voltage Spinel $LiNi_{0.44}Mn_{1.56}O_4$ with Fixed Oxygen Content

Burak Aktekin, Felix Massel, Majid Ahmadi, Mario Valvo, Maria Hahlin, Wolfgang Zipprich, Fernanda Marzano, Laurent Duda, Reza Younesi, Kristina Edström, and Daniel Brandell*

Cite This: *ACS Appl. Energy Mater.* 2020, 3, 6001−6013 Read Online

ACCESS | Metrics & More | Article Recommendations | Supporting Information

ABSTRACT: The crystal structure of $LiNi_{0.5}Mn_{1.5}O_4$ (LNMO) can adopt either low-symmetry ordered ($Fd\bar{3}m$) or high-symmetry disordered ($P4_332$) space group depending on the synthesis conditions. A majority of published studies agree on superior electrochemical performance of disordered LNMO, but the underlying reasons for improvement remain unclear due to the fact that different thermal history of the samples affects other material properties such as oxygen content and particle morphology. In this study, ordered and disordered samples were prepared with a new strategy that renders samples with identical properties apart from their cation ordering degree. This was achieved by heat treatment of powders under pure oxygen atmosphere at high temperature with a final annealing step at 710 °C for both samples, followed by slow or fast cooling. Electrochemical testing showed that cation disordering improves the stability of material in charged (delithiated) state and mitigates the impedance rise in LNMO||LTO ($Li_4Ti_5O_{12}$) and LNMO||Li cells. Through X-ray photoelectron spectroscopy (XPS), thicker surface films were observed on the ordered material, indicating more electrolyte side reactions. The ordered samples also showed significant changes in the Ni 2p XPS spectra, while the generation of ligand (oxygen) holes was observed in the Ni−O environment for both samples using X-ray absorption spectroscopy (XAS) and resonant inelastic X-ray scattering (RIXS). Moreover, high-resolution transmission electron microscopy (HRTEM) images indicated that the ordered samples show a decrease in ordering near the particle surface after cycling and a tendency toward rock-salt-like phase transformations. These results show that the structural arrangement of Mn/Ni (alone) has an effect on the surface and "near-surface" properties of LNMO, particularly in delithiated state, which is likely connected to the bulk electronic properties of this electrode material.

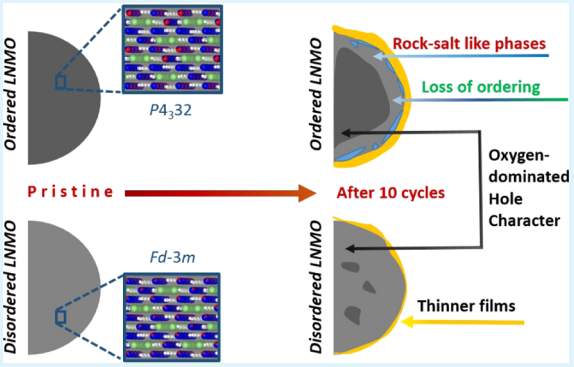

KEYWORDS: *high-voltage spinel, LNMO, cation ordering, oxygen deficiency, rock-salt, anionic redox*

INTRODUCTION

The development of lithium-ion batteries (LiBs) with high energy and power density has been of high interest in both industry and academia for several years. Among the cathode (positive electrode) alternatives for such LiBs, $LiNi_{0.5}Mn_{1.5}O_4$ (LNMO) is a promising spinel-type electrode material, since it has a high working potential around 4.7 V (vs Li^+/Li) arising from its Ni^{2+}/Ni^{4+} redox couple.[1] Another advantage of this material is its suitability for high-power applications, as Li^+ can easily move through interconnected tetrahedral sites (3D pathways) in the spinel framework.[2] However, even though satisfactory cycling results can be achieved in lab-scale half-cells, full cells still suffer from fast capacity fading, particularly at elevated temperatures.[3,4] To overcome this obstacle, it is crucial to understand the structure, dynamics, and reactivity of LNMO and their interplay with the electrochemical performance.

For the LNMO material, it is well known that synthesis and heat treatment conditions can change the cation (Mn/Ni) ordering in the crystal structure, resulting in low-symmetry ordered ($Fd\bar{3}m$) or high-symmetry disordered ($P4_332$) phases.[5] Despite some controversy on this topic, a majority of the published studies agree on a better electrochemical performance of the disordered phase,[6] and conditions favoring cation ordering, e.g., holding samples at 700 °C for long durations,[5,7,8] are therefore commonly avoided during the synthesis and postsynthesis treatment of LNMO powders.

To obtain the disordered LNMO phase, holding samples at high temperatures (>750 °C) is necessary.[6,7,9] However, oxygen release from the material also takes place in the same temperature region. The onset of oxygen release is observed at

Received: May 12, 2020
Accepted: May 13, 2020
Published: May 13, 2020

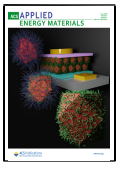

https://dx.doi.org/10.1021/acsaem.0c01075
ACS Appl. Energy Mater. 2020, 3, 6001−6013

temperatures above 700 °C, and the problem becomes gradually more severe by a further increase of the temperature.[10,11] Oxygen release can be compensated by the formation of oxygen vacancies[11] and/or rock-salt impurities, which possess a lower Mn/Ni ratio compared to the main spinel phase.[12] As a result, some of the Mn^{4+} in LNMO is reduced to Mn^{3+} to maintain charge neutrality. This means that some deviations in the stoichiometry should also be taken into account in comparative studies in the literature (e.g., $LiNi_{0.5}Mn_{1.5}O_4$ for the ordered LNMO vs $LiNi_{0.5-x}Mn_{1.5+x}O_{4-y}$ for the disordered LNMO). While the presence of Mn^{3+} has been considered to improve the electrochemical performance of the disordered phase due to increased electronic[13] and ionic conductivity,[14] more recent studies suggest that these advantages are limited to the higher lithiation states; when the entire range of lithiation/delithiation is considered, ordered and disordered samples show comparable rate capabilities.[15,16] It is important to note at this point that the better performance of the disordered phase is not explained by the cation disorder itself but rather by the oxygen release which takes place during sample preparation (and ensuring the presence of Mn^{3+}).

Alternative explanations have also been suggested, based on the hypothesis that cation disordering itself can affect how the phase transformations proceed during delithiation−lithiation. For instance, phase transformations in ordered LNMO have been shown to occur through successive two-phase transformations while solid-solution (single-phase) behavior at high lithiation states has been observed in disordered LNMO.[5,16−18] Therefore, a reduction in mechanical strain and kinetic barriers is possible during delithiation/lithiation for the disordered phase,[19] which can enhance cycling stability and rate capability. In this case, it may not be necessary to employ a fully disordered sample to obtain the benefits of disorder. A generally ordered sample, but with partial disordering, can still perform similar to a fully disordered sample with high Mn^{3+} content,[20] even if it does not display solid-solution behavior in the bulk—since partial disorder can still favor the formation of a solid-solution zone at the two-phase boundary.[16]

It is known that spinel cathodes are prone to instability issues in their delithiated (charged) state.[21,22] In a previous study,[23] we observed that conventionally prepared ordered and disordered samples show similar rate capability at the beginning of cycling; however, the differences in their performance evolve during battery operation. This evolution was found to be more dependent on the potentiostatic steps applied at the end of charging, indicating that the better performance of disordered LNMO is linked to an improved stability in its delithiated state. This observation does correspond less well with the established models for disordered LNMO's better stability—i.e., Mn^{3+} presence and solid-solution behavior—because in the delithiated state, all Mn^{3+} have been consumed and neither phase display any solid-solution behavior.

In light of these observations, it is reasonable to better explore the degradation processes that take place when the cathode is delithiated. This is also where the maximum electrode potential is reached, and thus severe electrolyte oxidation—and associated transition-metal dissolution—is expected. Moreover, near-surface structural reconstruction has been reported for delithiated spinel cathodes, e.g., $LiMn_2O_4$[24] and LNMO.[21] For the latter, transformations from the spinel to "Mn_3O_4-like" or "rock-salt-like" phases can occur locally near the surface and are possibly accompanied by oxygen release as well as transition-metal dissolution into the electrolyte.[21] Here, cation disordering itself, or other physical properties affected by high-temperature sample preparation, can have an impact on how severe these processes are. Additionally, in a separate study, we find that there is considerable oxygen participation in the charge compensation during the delithiation of ordered LNMO samples.[25] The formal cationic redox Ni^{2+}/Ni^{4+} has been shown to be a consequence of an electronic phase transition and oxygen hole formation (for example, see also the study by Mizokawa et al.[26] for $LiCoO_2$) via hybridization rather than of pure ionic nature. However, how Mn/Ni ordering affects such a redox activity, and its correlation to the electrochemical performance of LNMO, remains to be explored. In this context, the aforementioned degradation processes of disordered samples also need to be taken under consideration.

As stated earlier, ordered and disordered samples require different synthesis/heat treatment routes. This not only affects the Mn/Ni ordering but also causes changes in the Mn/Ni ratio,[12] formation of impurity phases,[11] introduction of oxygen vacancies,[11] and possibly renders changes in the particle size and facet morphology.[27] In situ neutron diffraction experiments[23] on Mn-rich LNMO powders showed no direct relationship between cation disordering and oxygen release: disordering can start prior to oxygen release under special conditions. The choice of slightly Mn-rich composition could also provide practical advantage during the preparation of oxygen-nondeficient disordered LNMO, e.g., by decreasing the tendency toward impurity phase formation. Following this insight,[23] i.e., targeting a temperature region above cation disordering (>680 °C) but still below oxygen release (<725 °C), we here anneal slightly Mn-rich micron-scaled crystallized powders in this temperature window to obtain both ordered and disordered samples. Both samples share a similar thermal history in terms of temperature and annealing time, except their cooling rates, which determine their ordering degree. Thanks to this strategy, ordered and disordered samples with the same amount of oxygen content and particle morphology have been studied for the first time with the aim to understand the individual effect of cation ordering on the electrochemical performance. The electrochemical performance is tested in LNMO-$Li_4Ti_5O_{12}$ (LTO) full cells and LNMO-Li half-cells. The cycled electrodes are also investigated ex situ using X-ray photoelectron spectroscopy (XPS), X-ray absorption spectroscopy (XAS), resonant inelastic X-ray scattering (RIXS), and high-resolution transmission electron microscopy (HRTEM) to elucidate the origins for the performance difference between these two structures.

EXPERIMENTAL SECTION

Sample Preparation. Following the observations made in our previous study,[23] 710 °C was selected as the annealing temperature (under pure oxygen atmosphere) to obtain both ordered (TMord) and disordered (TMdis) samples from micron-scaled $LiNi_{0.44}Mn_{1.56}O_4$ powders. Under these conditions, 710 °C is below the oxygen release temperature (<725 °C) but above the upper limit of temperature window for ordering−disordering transition (>680 °C). Powders were put into an alumina pan with inner dimensions 19 × 44 × 16 mm^3. In a tube furnace with an airtight quartz tube (under pure oxygen flow, which is ensured by airtight stainless steel flanges between tube ends and oxygen line), samples were first heated to 760 °C in 6 h. Thereafter, the temperature was decreased to 500 °C and then raised back to 760 °C. In each heating and cooling step, the

https://dx.doi.org/10.1021/acsaem.0c01075
ACS Appl. Energy Mater. 2020, 3, 6001−6013

duration was 2 h. This activation step was introduced to avoid any possible changes in the morphology and concentration of oxygen deficiencies, impurity phases, crystal defects, etc. during the final heat treatment step. In this final step, the temperature was decreased to 710 °C. At this temperature, the samples were kept for 2 h and should not be oxygen-deficient but free from impurities and adopt a disordered ($Fd\bar{3}m$) structure. To maintain cation disordering, the alumina pan was rapidly taken away from the furnace and the powders were dispersed on a large stainless plate (19 × 34 × 2.5 cm^3) for quenching. In this way, disordered (TMdis, $Fd\bar{3}m$) samples were prepared. To obtain ordered (TMord, $P4_332$) samples, the powders were slowly cooled to 310 °C in 10 h instead of quenching, and then the furnace was progressively cooled to room temperature. Thereby, both samples had the same thermal history except for their final cooling rate.

Characterization of Mn/Ni Ordering and Oxygen Content. Control and confirmation of ordering and disordering features were carried out via Raman spectroscopy using reference samples, which had been previously characterized by neutron diffraction.[23] The instrument employed here was a Raman microscope (Renishaw inVia) operated with a laser excitation wavelength of 532 nm and a ×50 lens objective. Preliminary calibration was performed using a monocrystalline Si sample to obtain a reference peak around 520.6 cm^{-1}. The number of acquisitions was 20, while the nominal laser power and the measuring time were 0.5 mW and 20 s for each measurement, respectively. Minimization of the laser beam exposure was applied for all of the samples in between subsequent acquisitions to prevent any possible detrimental effect on their surfaces. For thermogravimetric analysis (TGA), a "Q500-TGA" from TA Instruments was used. Analyses were done under pure oxygen flow with a platinum pan.

Electrochemical Testing. Composite electrodes comprised 90 wt % active material, 5 wt % carbon black (Imerys, C65) and 5 wt % poly(vinylidene difluoride)-based binder (PVdF-HFP; Kynar Flex 2801). The electrode diameter was 2 cm with an average capacity of 1.1−1.3 mAh/cm^2. As the counter electrode, either a Li metal (2.6 cm diameter and 125 μm thick, Cyprus Foote Minerals) or LTO ($Li_4Ti_5O_{12}$, Leclanché, 2 cm diameter, 1.7 mAh/cm^2 capacity) was used. The separator was either Celgard 2400 (in full cells) or Celgard 2325 (in half-cells). Electrodes and separators were dried in a vacuum furnace for 10 h inside a glovebox (Ar atmosphere, H_2O < 5 ppm, and O_2 < 1 ppm), in which the pouch cell assembly was also made. The electrolyte (120 μL for each cell) used was 1 M $LiPF_6$ (Ferro Corp.) dissolved in ethylene carbonate/diethyl carbonate (EC/DEC, 1:1 by volume, BASF). More details on the pouch cell assembly procedure can be found in an earlier work.[4] Cells were tested on a Novonix High Precision Charger (HPC) system at 55 °C. Cycling always started with a 10 h open-circuit voltage (OCV) step. In full cells, varying C-rates were chosen to test rate capability and constant voltage (CV) and OCV steps were added to test the material stability in the charged state. In half-cells, the charge/discharge rate was C/5. To ensure complete delithiation and to create more severe aging conditions, a 2 h CV step at 4.95 V (vs Li^+/Li) was added at the end of charging followed by a 2 h OCV step. For discharged samples, a CV step was added at 3.5 V (vs Li^+/Li) to ensure full lithiation. For further analyses, the cells were opened immediately in a glovebox. To prevent further self-discharge reactions, the electrodes were cleaned by dimethyl carbonate (DMC) three times (four to five droplets each) to remove any electrolyte residues.

Soft X-ray Spectroscopy. Transport of the air-sensitive LNMO electrode samples to synchrotron radiation facilities (ALS, and Spring-8, Japan) was carried out in airtight bags made of aluminum-laminated (pouch cell) films sealed under vacuum (30 mbar) in an argon glovebox (H_2O < 5 ppm and O_2 < 1 ppm). The samples were mounted with Cu tape on sample holders in an in-house argon glovebox and subsequently transferred to the endstation via an airtight suitcase, which was directly mountable on the ultrahigh-vacuum endstation. This procedure avoided any air exposure prior to the measurements.

Soft X-ray absorption spectroscopy (XAS) as well as resonant inelastic X-ray scattering (RIXS) measurements were performed. XAS spectra were collected for Mn L-, Ni L-, and O K-edge in partial fluorescence yield (PFY) mode and total electron yield (TEY) mode simultaneously, using an energy-resolving, liquid nitrogen-cooled, solid-state detector and by recording the sample drain current, respectively. PFY is bulk-sensitive with an average information depth of about 100 nm, while TEY mode is more surface-sensitive with an average information depth of about 10 nm. The monochromator bandwidth was set to 0.2 eV (O K-edge) and ∼0.3 eV (transition-metal L-edges). Ni L_3-edge and O K-RIXS measurements were performed using high-resolution, variable line space grating spectrometers. The combined instrumental (monochromator and spectrometer) resolution was 0.3 eV for O K-RIXS and 0.4 eV for Mn and Ni L-RIXS.

Following an established procedure,[28] all XAS spectra have been normalized by the incident intensity I_0, which was measured as drain current from an upstream Au-coated mesh. A linear background was fitted to the (mostly) flat regions below any absorption peaks and subsequently subtracted from each raw spectrum. Thereafter, normalization was done by setting the preedge flat region to zero and the postedge flat region to unity. To straightforwardly compare different spectral shapes, further individual normalizations have been applied for some data sets as detailed in the description of the different spectra.

XPS. Samples were cut into suitable size and placed onto double-sided Cu tape, which was attached to the XPS sample holder. Transfer to the XPS chamber was done via an airtight transfer system so that the samples were not exposed to air. The XPS instrument was a Phi-5500 with monochromatic Al-Kα radiation (1486.6 eV). The linear energy calibration was made so that the highest position of main Mn 2p peak was set to 642.3 eV,[4,29] and data analysis was made using Casa XPS software. Relative binding energy shifts of different surface components are known to occur at different state of charges (SOCs) within composite electrodes.[30] For this reason, the choice of hydrocarbon peak was not preferred for energy calibration in this study because of concerns over the accuracy of peak deconvolutions such as hydrocarbon and carbon black peaks (relative energy difference between these two peaks was not constant at different SOCs). Energy calibration was made using the LNMO component instead (i.e., a bulk reference point), and Mn 2p was chosen since it is expected to be less active compared to other elements throughout most of the delithiation process. Following Shirley background subtraction, data were normalized (divided by maximum) for each state of charge (SOC) for an easier comparison between ordered and disordered samples (except for the O 1s spectra of 1-EoC samples, where the maximum intensity in a region corresponding to surface species was chosen for the normalization). To enable an easier interpretation of spectra, one of the OCV spectra was chosen (disordered sample) and it was embedded in gray to each spectrum of subsequent SOC after normalizing at energies where bulk components are expected to be present.

TEM. The samples were dispersed in dimethyl carbonate (anhydrous ≥99%; Sigma-Aldrich) in a glovebox followed by ultrasonication for about 5 min. Then, a few drops of the solutions were drop-casted onto molybdenum TEM grids for electron microscopy investigation. A vacuum transfer double-tilt holder was used to transfer the grids from the glovebox to the microscope, to avoid air exposure. HRTEM investigations were carried out using a field-emission FEI Cs-corrected (image-corrected) cubed TitanTM microscope operating at 300 kV and equipped with a DE-16 direct electron camera.

RESULTS AND DISCUSSION

Preparation of Ordered and Disordered Samples with the Same Oxygen Content. As discussed earlier, the preparation of ordered and disordered samples generally requires different synthesis or heat treatment conditions (e.g., different atmospheres,[10] temperatures,[20] annealing

https://dx.doi.org/10.1021/acsaem.0c01075
ACS Appl. Energy Mater. 2020, 3, 6001−6013

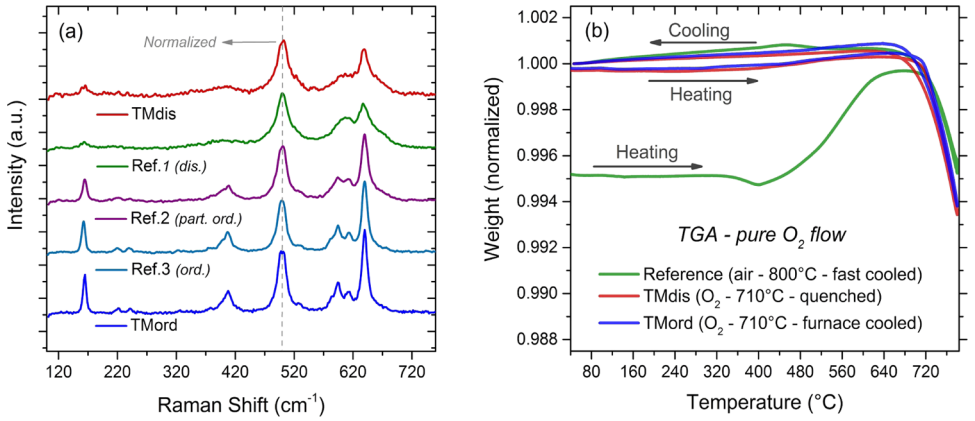

Figure 1. (a) Normalized Raman spectra of ordered (TMord) and disordered (TMdis) samples obtained in this study are shown together with spectra of reference samples with different degrees of ordering determined previously.[23] (b) TGA of ordered and disordered samples under oxygen atmosphere showing the amount of oxygen recovery after one heating/cooling cycle. The data for 800 °C (air-annealed sample)[23] are also shown for comparative purposes. All data are normalized (divided by final weight) so that the weight is equal at the end of cooling.

times,[16,31,32] etc.). These differences can also cause variations in the amount of oxygen released/recovered, the concentration of crystal defects, and/or the morphology and size of particles. As a consequence, the comparison of electrochemical performance will not uniquely show the effect of cation ordering/disordering but rather the effect of all material properties that varies due to differences in sample preparation. In this study, an alternative strategy has therefore been employed to obtain samples with cation ordering and disordering, which allows minimization of differences in other material properties, e.g., oxygen content. It has recently been shown through in situ neutron diffraction that cation disordering in LNMO can start prior to oxygen release during heating under specific conditions.[23] This means that at a certain temperature, it is possible to obtain cation disordering prior to oxygen release. Therefore, as described in the Experimental Section, both samples were subjected to identical thermal treatments under pure oxygen flow, in which the final step was at 710 °C. This temperature is above disordering but below oxygen release temperature.[23] Then, quenching vs slow cooling is expected to result in disordered vs ordered samples, respectively. The ordered ($P4_332$) phase is thermodynamically more favorable than the disordered ($Fd\bar{3}m$) counterpart at room temperature.[1] Therefore, slow or moderate cooling rates[23] should promote Mn/Ni ordering to take place in the structure. On the other hand, "freezing" of the disordered phase from 710 °C to room temperature via fast cooling is not straightforward for generating oxygen-nondeficient samples. Density functional theory (DFT) calculations have shown that oxygen deficiencies in the structure lower the energy difference between disordered and ordered structures[33,34] and thereby decrease the thermodynamical driving force toward the Mn/Ni ordering process. However, for the specific sample conditions in this study, i.e., cooling of disordered but oxygen-nondeficient sample from 710 °C, this thermodynamical driving force toward the ordering is likely still high. This means that the quenching rate may be critical to successfully freeze the cation disordering to room temperature. To determine if the quenching rate was sufficient, the synthesized powders were analyzed by Raman spectroscopy. In Figure 1a, Raman spectra of the samples are compared to those of reference specimens with varying degrees of ordering, which have previously been characterized by neutron diffraction.[23] The intensity ratio of the two most prominent peaks observed around 496 and 638 cm^{-1} should increase with increasing ordering in the samples,[35] while the peaks at 162 and 407 cm^{-1} correspond to Ni−O bands and also constitute an indication of cation ordering.[8,36] The comparison of the obtained spectra with those from reference samples clearly shows a successful preparation of ordered and disordered samples through the applied thermal treatment.

Since the powders are exposed to air for a very short time when they are removed from the furnace, it is necessary to confirm that no oxygen was released during the quenching process. The amount of initial oxygen content was therefore determined by TGA performed under pure oxygen flow during one heating and cooling cycle. The difference in weight before and after the analysis would correspond to the amount of oxygen recovered during this test, and therefore show the initial difference in the oxygen content of the powders. In Figure 1b, the results of ordered and disordered samples are shown together with a conventionally prepared disordered sample, which was annealed at 800 °C under air and then rapidly cooled. The data are normalized so that each sample has an equal weight at the end of the test (i.e., all data were divided by the final weight). The test shows that samples prepared in this study do not recover any considerable amount of oxygen during the TGA cycle and that the oxygen contents of both samples are similar. It is thereby confirmed that the ordered and disordered samples are successfully prepared using this novel preparation strategy,[23] which allows the control of cation ordering without any significant changes in other physical properties such as oxygen content or particle morphology (see Figure S1 for the SEM images of samples).

Effect of Cation (Mn/Ni) Ordering on Electrochemical Performance. Comparisons of the electrochemical performance of ordered (TMord) and disordered (TMdis) LNMO electrodes were made in full cells using LTO as the counter electrode. As shown in earlier studies,[4,23] this full cell chemistry has several advantages over half-cells employing Li metal as the counter electrode, primarily in terms of the rate capability testing and the ability to determine loss of cyclable Li caused by side reactions. Since the failure of LNMO-based cells is more severe at elevated temperatures, testing was performed at 55 °C, starting with galvanostatic cycling at C/2 charge and 10C discharge rates—note that 1C corresponds to charge/

https://dx.doi.org/10.1021/acsaem.0c01075
ACS Appl. Energy Mater. 2020, 3, 6001−6013

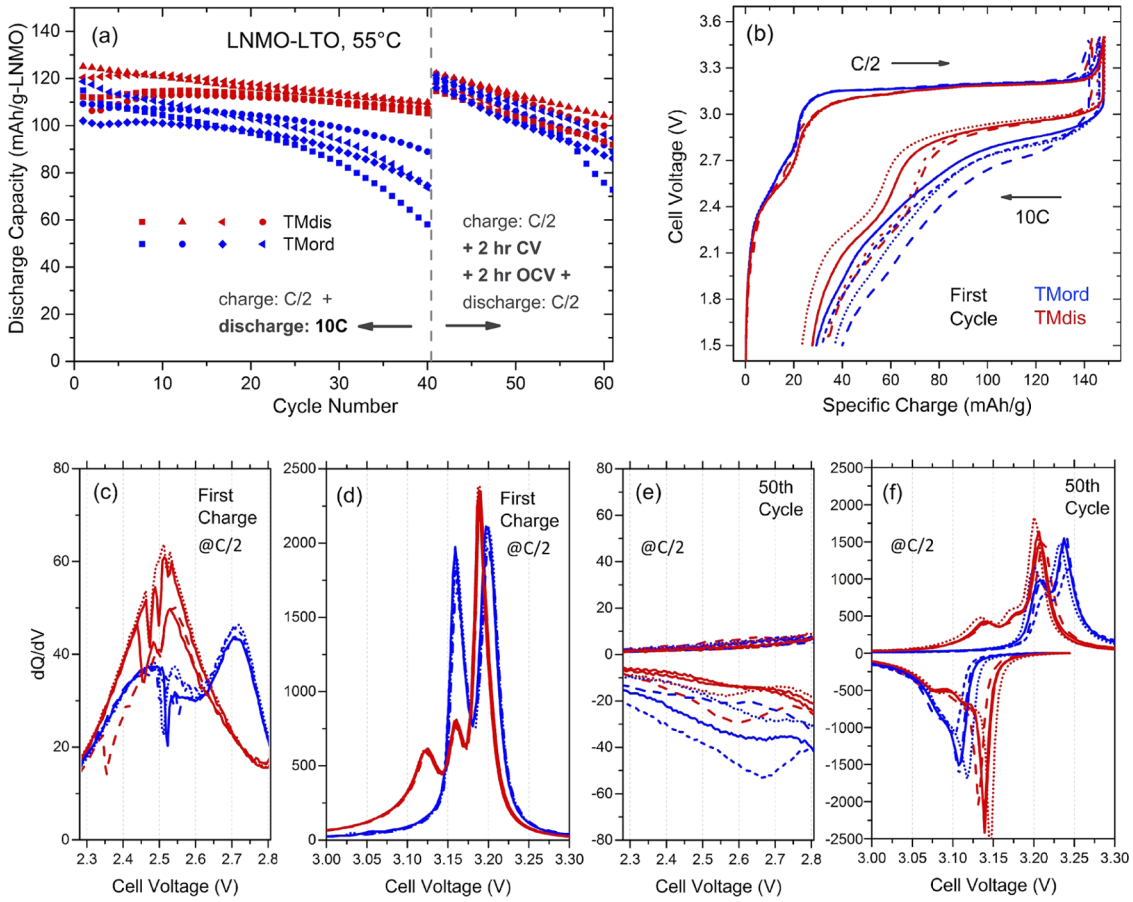

Figure 2. Electrochemical testing (at 55 °C) of ordered (TMord; blue) and disordered (TMdis, red) samples in LNMO-LTO full cells. Each sample has been tested in four different cells to assure reproducible results. These identical cells are shown with the same color, but different symbols and line shapes are used for each cell. (a) Discharge capacity vs cycle number. (b) Voltage curves from the first cycle. (c, d) Differential capacity plots for the first charge cycle (at C/2 rate) for the low- and high-voltage regions, respectively. (e, f) Differential capacity plots for the 50th cycle.

discharge in 1 h according to a theoretical capacity of 147 mAh g^{-1}. These C-rates, i.e., slow charging and fast discharging, were chosen considering the aim to investigate how intrinsic rate capabilities differ between samples. Side reactions can be expected to occur to a higher degree during charging, and fast charging would make such reactions more severe. Therefore, high rate was applied during discharge in this first part of the cycling since the aim was to investigate rate capability rather than high-voltage stability. After 40 cycles, the cycling was continued employing a different scheme: the charging rate was still C/2; however, a potentiostatic step was added for 2 h at the end of charging, followed by keeping the cells at OCV for 2 h. These steps at high voltage in the second part of the cycling make the cycling conditions quite severe in terms of side reactions, and were added to observe how the stability of the different electrodes varies in the charged (delithiated) state. Since high rates are tested, electrodes were subjected to high pressure (~160 MPa) before cell assembly to minimize the resistances in the composite electrodes.

As seen in Figure 2a, comparatively high discharge capacities around 110−120 mAh/g-LNMO were obtained for all samples at a 10C discharge rate, with the disordered samples displaying slightly higher capacity. In Figure 2b, individual voltage curves from the first cycle are shown. At C/2 charge rate, the voltage profiles are quite similar; however, the ordered samples show two plateau-like distinct features in the low-voltage region (see also Figure 2c) where the Mn^{3+}/Mn^{4+} transition occurs. Similar features have been reported for ordered Mn-rich samples[10,37] and it is here confirmed that the disappearance of such features does not occur due to oxygen deficiencies in the disordered samples, since both samples have the same oxygen content. This indicates that there are some changes in the electronic structure in the low-voltage region that are caused solely by cation ordering.

The region where the specific charge is above ~20 mAh/g-LNMO (i.e., the region where no Mn^{3+} is expected for this composition) shows higher voltages for the ordered samples, until the charge passed reaches 80−85 mAh/g-LNMO. Thereafter, the voltage curves seem quite similar. To investigate the region between 20 and 80 mAh/g-LNMO better, differential capacity plots were obtained and are presented in Figure 2d. The ordered samples show two intense peaks located at 3.16 and 3.20 V. The disordered samples also display these features but at slightly lower potentials (3.19 V for the highest peak), which can be due to a slightly higher overpotential of the ordered electrodes. In earlier studies, in which the oxygen content also possibly varied, a shift of the second largest peak (at 3.16 V) to lower voltage has been reported.[5,38,39] Here, this peak instead decreases in intensity and a third peak at lower voltage appears, which can be due to different arrangement of occupied vs vacant Li sites in this voltage region.[40] Since

https://dx.doi.org/10.1021/acsaem.0c01075
ACS Appl. Energy Mater. 2020, 3, 6001−6013

internal cell resistance and testing rates can vary considerably in the literature, it is difficult to draw any firm conclusions by comparing these observations to the literature, and the effect of oxygen content vs disordering should in future studies be observed under identical testing conditions.

As seen in Figure 2a, both samples are able to initially deliver high capacities when discharged at the 10C rate. In the first cycle, despite that the discharge capacities are quite similar, the voltage curves during discharge (Figure 2b) appear quite different as the ordered samples display less of a plateau-like profile and a higher overpotential. This indicates that there are differences in the delithiation/lithiation mechanisms already in the first cycle, but considering the similarities in capacity during the first cycle, this effect is not significant enough to explain the differences in capacity retention over extended cycling. As the cycling continues, the disordered samples maintain the initial capacities while the ordered samples show a gradual decrease of capacity. Since the discharge rate applied in this first part of the cycling is high, the discharge capacities should be highly sensitive to the cell resistance. It is observed that the disordered samples are more stable against such a resistance increase. In the second part of the cycling, when the discharge rate is decreased to C/2, both samples recover their capacities up to 120 mAh/g-LNMO. This confirms that the previously observed capacity decrease of the ordered sample at 10C rate is mainly caused by the higher cell resistance. In the second part of the cycling, however, severe capacity fading occurs but in a similar manner for both ordered and disordered samples. This is due to side reactions, and the capacity decrease is dominated by cyclable lithium loss,[4] which is also confirmed in Figure 2e by the area decrease of the low-voltage peaks. Severe cyclable lithium loss is expected here as a result of the potentiostatic and OCV steps intentionally added at the higher voltage. It can be assumed that these side reactions can cause a higher degree of cell resistance in this second part of the cycling but without affecting the discharge capacity because of the slow rate cycling and potentiostatic steps. Therefore, differential capacity plots can be more informative than observing the capacity retention when investigating such a resistance increase. As can be seen in Figure 2f, the disordered samples display minimal peak shifts, while considerable shifts occur for the ordered samples, thereby signaling a better chemical stability. The differential capacity plots for the 42nd and 58th cycles are given in the Supplementary Information (see Figure S2), which further confirm that a significant impedance rise occurs during the later part of the cycling for the ordered samples.

In conclusion, cation (Mn/Ni) disordering is seen to mitigate the impedance growth, which occurs and severely affects the electrochemical performance in the charged state of the cell. The results do not, however, indicate any considerable difference in terms of the side reactions, which cause loss of cyclable lithium. To get more insight on the reasons behind this observation, ex situ characterization of cycled LNMO electrodes was performed at different SOC levels.

Preparation of Samples in Half-Cells for Ex Situ Characterization. Samples were prepared in half-cells (55 °C) to ensure full lithiation and delithiation of the LNMO electrodes. Ordered and disordered samples were cycled 10 times, and during the last half-cycle, i.e., the 11th cycle, the cells were stopped in their charged state. Since the aim was to investigate the degradation in the charged (delithiated) state, CV and OCV steps were added at the end of each charging cycle. Voltage curves from the 1st and the 10th and 11th cycles are shown in Figure 3a,b, respectively (see Figure S3 for

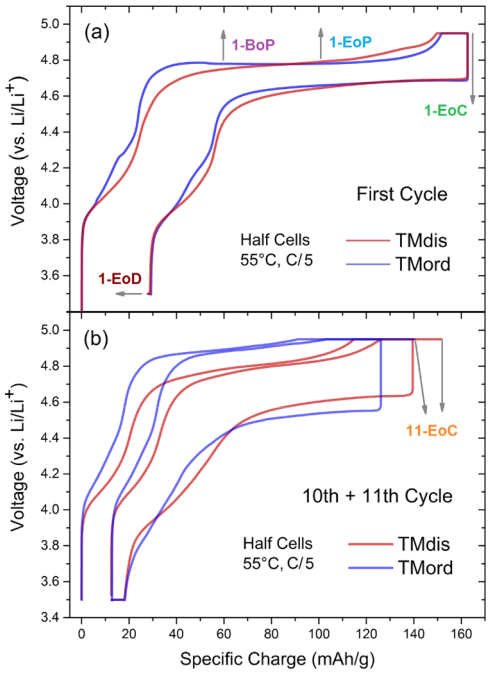

Figure 3. Voltage curves from LNMO-Li half-cells cycled for 10 full cycles + 1 half-cycle. (a) The first cycle and (b) the 10th and 11th cycles. Additional cells were prepared to obtain samples at different SOCs in the first cycle (see Figure S4); the positions of SOC for these samples are indicated by arrows in (a).

capacity vs cycle number and coulombic efficiency (CE) vs cycle number graphs). Similar CEs for both samples can be observed, but the main difference between the cells is the different degree of increase in overpotential during cycling, which is in accordance with the observations in full cells. Additional cells were prepared, and each one of them was stopped at different SOCs during the first cycle—Beginning of Plateau (BoP), End of Plateau (EoP), End of Charge (EoC), and End of Discharge (EoD). The positions of these samples are shown in Figure 3a (arrows), and the individual voltage curves for each cell are given in Figure S4.

X-ray Photoelectron Spectroscopy (XPS). Electrolyte oxidation at high potential and transition-metal dissolution from the active material are widely recognized problems for the LNMO material. Due to its surface sensitivity, XPS is a valuable tool to obtain information on the resulting reaction products deposited on the surface of the active material as well as inactive electrode components. In this section, the electrodes cycled in half-cell configuration to different SOC levels in the first cycle are analyzed. Since the differences in electrochemical performance mainly evolve during cycling, analysis of electrodes after 10 1/2 cycles (with CV steps in charged state to render more severe conditions) is also provided. XPS results for the C 1s, O 1s, and Ni 2p are shown in Figure 4 together with the relative atomic percentages of the analyzed elements. Differences for Mn 2p, F 1s, and P 2p spectra were subtle and are provided in Figure S5.

In the C 1s spectra (Figure 4a), both ordered and disordered samples show very similar behavior after the OCV period apart from subtle differences in the region where C−O-related species (286.7 eV) are expected. With charging (delithiation)

https://dx.doi.org/10.1021/acsaem.0c01075
ACS Appl. Energy Mater. 2020, 3, 6001−6013

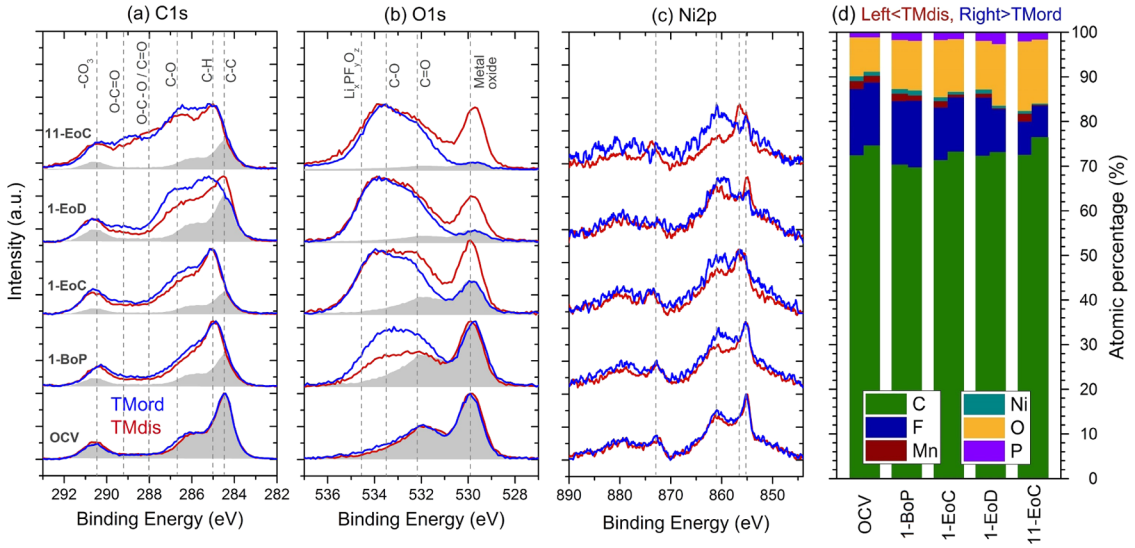

Figure 4. XPS results of cycled LNMO electrodes (at 55 °C) harvested from half-cells at different SOC levels (as shown in Figure 3). Normalized spectra for C 1s, O 1s, and Ni 2p are shown in (a–c), respectively. Spectrum of OCV sample (disordered) is shown in gray to enable an easier comparison (its intensity is normalized with the parts of the spectrum where bulk components are present). Relative atomic percentages of the analyzed elements are given in (d). In this figure, the left part of the bars corresponds to atomic percentages of disordered samples, while the right part is for ordered samples. "OCV" samples are obtained by electrodes harvested from half-cells after 10 h waiting time at 55 °C, but without applying any current.

of the LNMO electrodes, organic species start to deposit on both electrodes, which is seen from that the relative intensity in the binding energy region between C−H and $-CO_3$ increases significantly relative to the C−C (to observe these changes easier, one of the spectra from OCV samples was embedded for each SOC). During the charging, the difference between ordered and disordered samples is mainly observed in the C−O region, and it seems that cation ordering favors the formation of C−O-rich surface films.

After one cycle (including CV and OCV steps), the differences between ordered and disordered samples become more pronounced. It is clear for both samples that the coverage of carbon black particles by surface deposits is smaller after one full cycle compared to one half-cycle. This implies that the surface layer is reduced in thickness during discharging. Interestingly, this is relatively less notable for the ordered sample, which thus seems to form a more robust surface layer.

In the O 1s (Figure 4b) spectra, similar trends are also observed, where organic and inorganic species for the ordered samples form to a larger degree on electrodes. This is seen from the increase in the relative ratio of the surface-related peaks (e.g., $Li_xPF_yO_z$ at 534.6 eV, C−O at 533.5 eV, and C═O at 532.2 eV) to the lattice metal oxide peak (around 529.9 eV). As is clear from the O 1s spectra, significant film growth occurs for both samples during the full first cycle, although the film is thicker on the ordered sample. For the ordered sample, the surface layer buildup increases with cycling up to the 11th cycle. However, for the disordered sample, the surface layer in the first charged state is similar to that on the 11th cycle. For all SOCs, the relative changes observed between the ordered and disordered samples are more severe in the O 1s region compared to the C 1s region, indicating the inhomogeneous distribution of surface deposits. This can be caused by additional side reactions occurring on the active material of ordered electrodes. There is also the possibility of oxygen vacancy formation being the cause of relative decrease in intensity from metal oxide peaks. However, the trends in the intensity of other elements in the bulk (Mn and Ni) are similar to that of M−O in O 1s, and therefore oxygen vacancies are not likely the reason (for this observation, see Figure S6 for the raw spectra of C 1s, O 1s, Mn 2p, and Ni 2p before and after cycling).

In the Mn 2p spectra (Figure S5a), both samples show the same behavior. Moreover, the line shapes seem identical during delithiation, except for the disappearance of a small component at a low binding energy. This is a good indication of oxidation of Mn^{3+} to Mn^{4+} during the early stage of charging, since this component is not part of the Mn^{4+} multiplet structure.[41] In contrast to Mn 2p, considerable changes are instead observed in the Ni 2p spectra for different SOC levels of the electrodes (Figure 4c). In the first cycle, the highest position of the Ni $2p_{3/2}$ multiplet peak (~855.2 eV) remains constant in binding energy from OCV to 1-BoP but shifts around 1.4 eV to a higher energy (~856.6 eV) at the end of charging. During the following discharge, it returns to its original position, indicating that this 1.4 eV shift is due to Ni oxidation/reduction. Such a shift has previously been assigned to the oxidation of Ni^{2+} to the Ni^{4+} state[42] or to the Ni^{3+} state[43] for layered oxides. It is not possible to determine the oxidation state of nickel with any high accuracy since there are also other factors such as the complexity of multiplet structure,[44] the possible contributions from nickel dissolution and subsequent incorporation into the organic surface film, and overlapping Auger emissions from F (KL_1L_{23}) and Mn ($L_3M_{45}M_{45}$) (with Al Kα radiation).

Apart from the apparent shift of Ni $2p_{3/2}$ multiplet peak, peak broadening is also observed as the sample is fully delithiated. The intensity of the main satellite peak also increases with charging, but this seems to be nonreversible and the trend continues with cycling. This behavior differs between the samples, and the increase in intensity appears to a higher extent for the ordered samples. Such changes can be related to the formation of defects, such as oxygen vacancies,[45] even though significant formation of oxygen vacancies is not

https://dx.doi.org/10.1021/acsaem.0c01075
ACS Appl. Energy Mater. 2020, 3, 6001−6013

expected. These changes can also be related to differences in covalency[44,46] with the oxygen atoms.

In summary, these XPS results show that side reactions and film formation on LNMO occur to a higher extent on ordered LNMO surfaces. To get more insight into the differences between two samples, XAS and RIXS measurements were performed to probe changes in electronic structure in the bulk of the material.

XAS/RIXS. It is observed that manganese plays a negligible role in the redox mechanism, which may be expected from the stoichiometry of the pristine materials in which manganese already has a high oxidation state. Figure S7 shows that the spectral shape of Mn L-XAS changes very little from the Mn^{4+}-dominated signature[47] of the pristine state, with the exception of minor spectral changes in the low-voltage region around 4.2 V (vs Li^+/Li), possibly indicating the $Mn^{3+/4+}$ redox of a small minority of ions. This is expected[48] and in accordance with the trends of Mn 2p XPS spectra (see Figure S5). After consecutive cycling, an increase of Mn^{2+} and Mn^{3+} contributions is observed in the surface-sensitive signal of the delithiated material (11-EoC), which can arise from the presence of dissolved TMs incorporated into the surface film.

Figure 5a shows the evolution of the Ni L_3-XAS spectra in the PFY mode upon cycling of the two materials to several

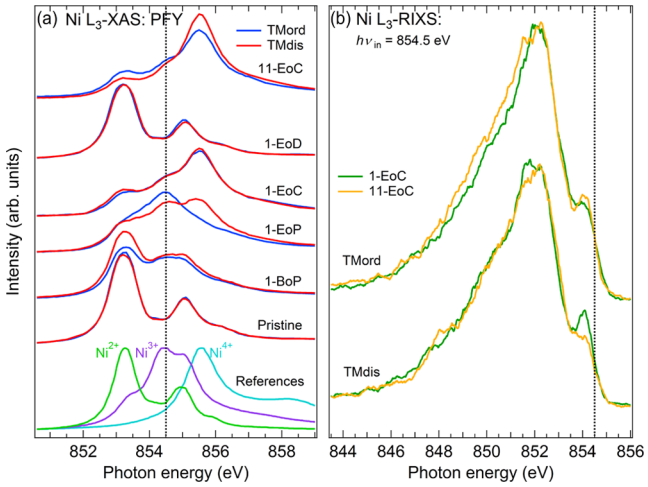

Figure 5. (a) Ni L_3-edge XAS in PFY signal of cycled LNMO electrodes harvested from half-cells at different SOCs. Reference spectra as reported by Qiao et al.[49] (b) Ni L_3-edge RIXS at an incident photon energy of 854.5 eV of the 1st and 11th cycle delithiated SOC.

SOCs during the first cycle and to fully delithiated SOC of the 11th cycle. For comparison, calculations of Ni L_3-XAS spectra with various Ni oxidation states are here shown as previously reported by Qiao et al.[49] The comparison clearly reveals a dominant Ni^{2+} oxidation state in the pristine materials. The spectra of the increasingly delithiated states 1-BoP, 1-EoP, and 1-EoC exhibit progressively more admixtures of the higher oxidation states Ni^{3+} and Ni^{4+}.[50] Upon relithiation of the materials to 1-EoD, the spectral shapes return to that of Ni^{2+}, indicating a largely reversible redox mechanism centered around Ni in the first cycle. Finally, the spectra for the materials that have been delithiated for the 11th time (11-EoC) are shown at the top of Figure 5a.

While we can acknowledge the strong overall similarities between the spectral behaviors, interestingly, differences between the two materials manifest themselves particularly at 1-EoP and 11-EoC. While the spectra of both materials at 1-EoP exhibit strong signatures corresponding to those of the Ni^{3+} standard (see the vertical dashed line in Figure 5a), the TMdis spectrum has an additional, most intense feature at 855.5 eV corresponding to the main feature of the Ni^{4+} reference. This means that Ni ions in the disordered material reach their highest oxidation state earlier in the delithiation cycle compared to the ordered material. Upon further delithiation to 1-EoC, Ni oxidation continues and the ordered material catches up so that both materials end up with virtually congruent spectra. However, after the 11th delithiation to 11-EoC, this is no longer the case, instead the behaviors of both materials diverge. Upon repeated cycling to 11-EoC, the disordered material contains somewhat more highly oxidized Ni ions, while the ordered material retains the ratio between the Ni L_3 main absorption features observed at 1-EoC.

Figure 5b shows Ni L_3-RIXS spectra of all delithiated samples (1-EoC and 11-EoC) at an incident photon energy of 854.5 eV corresponding to the Ni^{3+}-centroid. Both materials show an extended "tail" at energies lower than the peak. It is known[51,52] that this feature is due to so-called charge transfer states that are related to holes in the oxygen band. In a related study, we show that charge compensation in LNMO is best described, not as a purely ionic Ni redox process, but rather driven by redox processes in a Ni−O-hybridized band of strong oxygen character undergoing an electronic phase transition.[25] Thus, it is important to closely compare the O K-RIXS spectra of both materials in order to obtain a complete picture.

Figure 6a shows a combination of O K-edge RIXS and XAS spectra reflecting the changes throughout the first delithiation

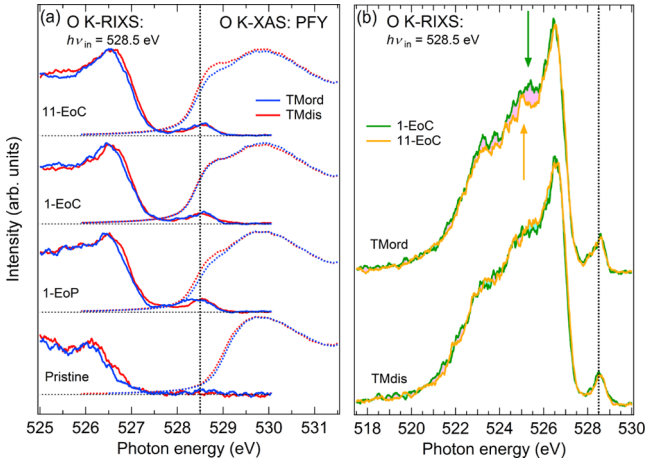

Figure 6. (a) O K-edge RIXS (left, solid traces) and PFY signal XAS (right, dashed traces) of selected SOC of the ordered and disordered materials in direct comparison. The vertical dashed line marks the RIXS incident photon energy of 528.5 eV. (b) O K-edge RIXS spectra at the incident photon energy 528.5 eV comparing the delithiated samples of the 1st and 11th cycles, green and yellow, respectively, of ordered and disordered materials, respectively. All RIXS spectra are normalized for matching low-energy flanks.

that occur in the occupied and unoccupied O 2p-bands, respectively. The preedge of the XAS (528−535 eV) reflects Ni 3d−O 2p hybridized states that acquire extra holes upon delithiation that are reflected by the development of a distinct preedge shoulder (increase of intensity around the dashed

https://dx.doi.org/10.1021/acsaem.0c01075
ACS Appl. Energy Mater. 2020, 3, 6001−6013

vertical line) close to the Fermi level, which is located within ~0.5 eV below the dashed vertical line. This occurs for both materials, whereas the prominence of the preedge shoulder displays differences at certain SOC, namely, 1-EOP and 11-EOC.

The O K-RIXS spectra are characterized by the development of a distinct feature at the top of the main band (526.5 eV) with delithiation. Note that the vertical dashed line marks the incident energy (528.5 eV) for the presented RIXS spectra. This probes excitations into the developing preedge shoulder where one could expect differences to manifest themselves at the earliest cycling stages. The overall evolution is similar, yet an interesting difference between the materials is manifested by the changes of states directly at the Fermi level seen as a small "elastic peak" in the 1-EoP spectra. At 1-EoP, the disordered material exhibits fewer occupied states within about 1 eV of the Fermi level compared to the ordered material. This coincides with the observation in the Ni XAS, in which we observe a more advanced Ni oxidation in the disordered material at this particular SOC. As seen above, this effect equalizes when reaching the end of the first charge (1-EoC), yet it has a long-term effect on the material (11-EoC). This kind of long-term effect is also seen in the O K-RIXS spectra (Figure 6b, upper two comparisons), where the ordered material clearly undergoes a development (viz., arrows pointing out the difference in the ratio between the top of the band and the main band), whereas the disordered material shows less spectral change. Note also that the elastic peak of the ordered material shows a similar asymmetry at both 1-EoC and 11-EoC to that at 1-EoP. We can thus summarize the XAS/RIXS results by noting the tendency of the disordered material to reach a higher degree of Ni oxidation at an earlier SOC in the first cycle and to have a more stable long-term electronic structure in the delithiated state than the ordered material, which tends to acquire fewer holes on the O ions than the disordered material. This behavior on the microscopic level could be conducive to a more stable battery cycling performance on the macroscopic scale.

HRTEM. Surface-sensitive characterizations of different LNMO samples were performed with XPS, while (relatively) bulk characterization was obtained using the XAS/RIXS technique. To observe "near-surface" changes in the crystal structure, the HRTEM technique was applied. Half-cells with ordered and disordered electrodes were cycled similarly for 10 1/2 cycles with CV steps in the charged state to render more severe aging conditions. The results from these cycled cells are shown in Figure 7, and the results from electrodes prior to any electrochemical cycling are shown in Figure S8. As seen in Figure S8a, the ordered material shows additional superstructure spots in the fast Fourier transform (FFT) image, as reported previously.[32] Here, these spots arise from the periodicity in the (110) planes. This is due to increasing Mn/Ni ordering, which causes this periodicity of Ni-rich layers separated by a 0.58 nm distance. As seen in Figure S8b, superstructure-related spots are not present in the disordered samples since the random mixing of Mn/Ni reduces the periodicity to the (220) planes. While the images are chosen in such a way that they are representative of general trends, it should be pointed out that there were some variations in the intensity of spots in FFT images (see Figure S9 for additional HRTEM images from each sample).

In Figure 7a, an HRTEM image of the ordered sample after cycling is shown. It is seen that structural changes occurred

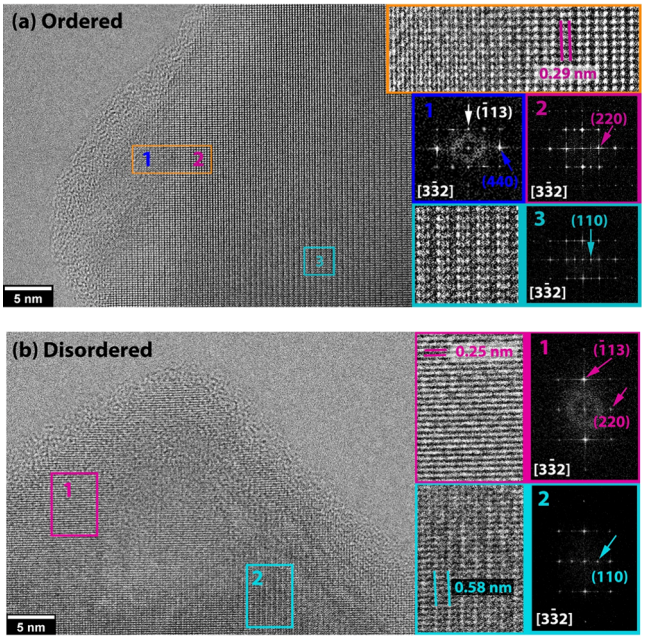

Figure 7. HRTEM images of ordered (a) and disordered (b) samples after cycling (after 10 1/2 cycles). Zoomed-in images from selected regions are shown in insets with their corresponding FFT images.

during cycling as significant differences are observed in the FFT images obtained from the different regions through the image. The inner regions (e.g., the cyan rectangle) clearly show the presence of extra superstructure spots due to (110) planes (see Figure S10 for the projected view of structure in the same zone axis with the image). In regions closer to the surface, the brightness of extra spots decreases and thus indicates a decrease in ordering. In regions just below the surface, i.e., near surface, domains with rock-salt character are observed. In the zoomed-in view of the orange rectangle, the transition from the spinel to the rock-salt-like phase is easily seen, which is likely caused by the occupancy of empty octahedral sites in the structure. The FFT image from the rock-salt region (#1, blue) shows an increase in (440) spots, while (110) spots disappear and (220) spots decrease in brightness. This clearly shows the loss of ordering and the formation of rock-salt-like phases. In cycled ordered samples, when going from inner regions to the surface, the general trend was first a decrease in ordering and then a complete loss of ordering, together with some observed domains in which (440) spots had a higher brightness compared to (220) spots. Additional images are shown in Figure S11. This again indicates rock-salt-like surface reconstruction to varying degrees. In the disordered samples (see Figure 7b), on the other hand, such regions with a high rock-salt-like character were not observed. Surprisingly, it was possible to see some degree of ordering in the inner regions of the particles, which was not present before cycling. Since disordered samples used in this study have been prepared with a new strategy (without oxygen deficiency), the driving force for cation ordering would be expected to be high. Accordingly, it is possible that the inner regions could partially adopt cation ordering during lithiation−delithiation cycles at elevated temperature. This would not be expected in the near-surface regions as any oxygen release and near-surface reconstruction would decrease such a driving force for cation ordering.

In summary, samples were characterized ex situ using different techniques. With the surface-sensitive XPS technique,

https://dx.doi.org/10.1021/acsaem.0c01075
ACS Appl. Energy Mater. 2020, 3, 6001−6013

thicker surface deposits were observed on ordered electrodes already during the first charging. This difference can originate from changes in the bulk electronic structure. It was observed from the XAS/RIXS characterization that both samples are subject to a considerable formation of holes on oxygen in the Ni−O environment. This is expected to influence the chemical reactivity of carbonate-based electrolytes on the active material surface.[53] However, when comparing the spectral details of the two samples, the ordered material was observed to acquire a relatively lower number of holes on oxygen. If the surface film thickness is assumed to reflect the extent of side reactions, this would mean that other side reactions should also be at play on the LNMO surface. Since anionic processes take part in charge compensation, the possibility of lattice oxygen release[54] needs also to be considered. In the case of the ordered sample, HRTEM observations showed that phase transformations to rock-salt-like phases occur near the surface, which is possibly accompanied by some oxygen release from the lattice. Such a release, e.g., in the form of singlet oxygen, could cause further chemical reactions inside the cell[55,56] and result in thicker surface film formation on electrodes. Prior to oxygen release, oxygen vacancies can also be formed,[57] and at this point, it is necessary to confirm that the decrease of the metal oxide peak in Figure 4b was not caused by the formation of vacancies. As seen from the XPS results in Figure S6, given without any normalization, trends of O, Mn, and Ni are in agreement with each other, thereby supporting that thicker films are indeed formed on the ordered material. This is further supported by HRTEM images.

Previously, oxygen release has not been considered to occur extensively for LNMO;[58,59] however, our observations indicate its occurrence, particularly for the ordered material. This can be interpreted as that the presence of neighboring NiO_6 octahedra in disordered structure is surprisingly beneficial for the stability of oxygen hole states, especially in delithiated states. In this part, important observations that can explain the impedance rise in cells with ordered LNMO electrodes were made via ex situ characterization; however, further experimental and computational investigations of delithiated LNMO need to be performed in the future to elucidate the fundamental relationships between these observations, i.e., changes in the electronic structure, side reactions, and near-surface phase transformations.

CONCLUSIONS

In this study, the effect of cation disordering on the electrochemical performance of LNMO has been studied in a controlled way by decoupling the effect of disordering from other material properties. A final heat treatment step is applied at 710 °C under a pure oxygen atmosphere for the same duration for both samples, making the cooling rate the only distinctive parameter to obtain ordered and disordered samples without affecting their oxygen content or particle morphology. Electrochemical testing at 55 °C in full and half-cells shows that disordering (alone) helps to maintain cycling performance, particularly due to a better stability of the disordered sample in the delithiated state. Therefore, although there have been clear indications of beneficial effects of disordering for a long time, this study provides stronger evidence for this effect, while at the same time rendering it possible to draw firm conclusions on the chemical background of this phenomenon.

Electrochemical testing of ordered and disordered samples show that their initial rate capabilities are similar and that side reactions cause loss of cyclable lithium in a comparable way, but with a more extensive impedance rise for the ordered sample. This is partly explained by the XPS analysis of cycled electrodes, which shows thicker film formation on ordered material surface during charging with more deposition of C−O, C═O, and $Li_xPF_yO_z$ species. At the same time, the XAS/RIXS characterization of the particles shows small but significant differences in the electronic structure during the first charge as well as after prolonged cycling. During charging, the ordered sample is subject to a somewhat delayed Ni−O band oxidation, an indication that seems to be confirmed also by small spectral differences between the delithiated states after 10 cycles. The tendency of delayed/reduced oxidation in the ordered sample could have an effect on its electrochemical performance, either directly or through additional side reactions. The latter could also result in the thicker film formation observed by XPS. The investigation of the local structural changes with HRTEM reveals loss of ordering and formation of rock-salt-like phase domains near the particle surface, as observed to occur more severely for the ordered material. Even though oxygen release during electrochemical cycling is usually not considered for the LNMO material, these results indicate that it might well occur at low rates and result in the chemical oxidation of the electrolyte. These findings could be decisive for designing improved high-voltage cathodes.

ASSOCIATED CONTENT

Supporting Information

The Supporting Information is available free of charge at https://pubs.acs.org/doi/10.1021/acsaem.0c01075.

Scanning electron microscopy (SEM) images of ordered (TMord) and disordered (TMdis) samples (Figure S1); selected voltage curves for the 42nd, 50th, and 58th cycles in Figure 2a (Figure S2); discharge capacity and coulombic efficiency vs cycle number graph for the cells cycled 10 1/2 times for the ex situ characterization of ordered and disordered LNMO electrodes (Figure S3); voltage curves of individual cells used for ex situ sample preparation of ordered and disordered samples (Figure S4); XPS results of cycled LNMO electrodes for Mn 2p, F 1s, and P 2p (Figure S5); XPS spectra of LNMO electrodes before and after cycling before any intensity normalization and background subtraction (Figure S6); Mn L3-edge XAS spectra (TEY mode) for ordered and disordered samples at different states of charge (SOCs) (Figure S7); HRTEM images for ordered and disordered LNMO samples before cycling (Figure S8); additional HRTEM images for ordered and disordered LNMO samples before cycling (Figure S9); projected view of the ordered LNMO structure as seen from the same zone axis in HRTEM images in Figure 7 (Figure S10); and additional HRTEM images of ordered and disordered samples after cycling (Figure S11) (PDF)

AUTHOR INFORMATION

Corresponding Author

Daniel Brandell − *Department of Chemistry - Ångström Laboratory, Uppsala University, SE-75121 Uppsala, Sweden;* orcid.org/0000-0002-8019-2801; Email: daniel.brandell@kemi.uu.se

https://dx.doi.org/10.1021/acsaem.0c01075
ACS Appl. Energy Mater. 2020, 3, 6001−6013

Authors

Burak Aktekin − *Department of Chemistry - Ångström Laboratory, Uppsala University, SE-75121 Uppsala, Sweden*

Felix Massel − *Department of Physics and Astronomy, Division of Molecular and Condensed Matter Physics, Uppsala University, S-751 20 Uppsala, Sweden;* orcid.org/0000-0002-6537-1414

Majid Ahmadi − *Kavli Institute of Nanoscience, Faculty of Applied Sciences, Delft University of Technology, 2628 CJ Delft, The Netherlands;* orcid.org/0000-0003-2321-3060

Mario Valvo − *Department of Chemistry - Ångström Laboratory, Uppsala University, SE-75121 Uppsala, Sweden;* orcid.org/0000-0002-0069-8707

Maria Hahlin − *Department of Physics and Astronomy, Division of Molecular and Condensed Matter Physics, Uppsala University, S-751 20 Uppsala, Sweden;* orcid.org/0000-0002-5680-1216

Wolfgang Zipprich − *Volkswagen AG, D-38436 Wolfsburg, Germany*

Fernanda Marzano − *Scania CV AB, SE-151 87 Södertälje, Sweden*

Laurent Duda − *Department of Physics and Astronomy, Division of Molecular and Condensed Matter Physics, Uppsala University, S-751 20 Uppsala, Sweden;* orcid.org/0000-0001-8471-0955

Reza Younesi − *Department of Chemistry - Ångström Laboratory, Uppsala University, SE-75121 Uppsala, Sweden;* orcid.org/0000-0003-2538-8104

Kristina Edström − *Department of Chemistry - Ångström Laboratory, Uppsala University, SE-75121 Uppsala, Sweden;* orcid.org/0000-0003-4440-2952

Complete contact information is available at: https://pubs.acs.org/10.1021/acsaem.0c01075

Notes

The authors declare no competing financial interest.

■ ACKNOWLEDGMENTS

Volkswagen AG and Scania CV AB are acknowledged for the financial support of this work. The Swedish Energy Agency (project no. 42031−1) and StandUp for Energy are also acknowledged. Leclanché is acknowledged for the LTO electrodes used in full cells. M.V. gratefully acknowledges the funding from the Swedish Energy Agency (project no. 45510−1) and the ÅForsk Foundation (project no. 18−317). The authors thank the Advanced Light Source of Lawrence Berkeley National Laboratory for the beam time provided for XAS/RIXS measurements.

■ REFERENCES

(1) Li, W.; Song, B.; Manthiram, A. High-Voltage Positive Electrode Materials for Lithium-Ion Batteries. *Chem. Soc. Rev.* **2017**, *46*, 3006−3059.

(2) Kraytsberg, A.; Ein-Eli, Y. Higher, Stronger, Better... A Review of 5 Volt Cathode Materials for Advanced Lithium-Ion Batteries. *Adv. Energy Mater.* **2012**, *2*, 922−939.

(3) Kim, J. H.; Pieczonka, N. P. W.; Li, Z.; Wu, Y.; Harris, S.; Powell, B. R. Understanding the Capacity Fading Mechanism in LiNi0.5Mn 1.5O4/Graphite Li-Ion Batteries. *Electrochim. Acta* **2013**, *90*, 556−562.

(4) Aktekin, B.; Lacey, M. J.; Nordh, T.; Younesi, R.; Tengstedt, C.; Zipprich, W.; Brandell, D.; Edström, K. Understanding the Capacity Loss in LiNi $_{0.5}$ Mn $_{1.5}$ O $_{4}$ −Li $_{4}$ Ti $_{5}$ O $_{12}$ Lithium-Ion Cells at Ambient and Elevated Temperatures. *J. Phys. Chem. C* **2018**, *122*, 11234−11248.

(5) Kim, J.-H.; Myung, S.-T.; Yoon, C. S.; Kang, S. G.; Sun, Y.-K. Comparative Study of LiNi0.5Mn1.5O4-δ and LiNi0.5Mn1.5O4 Cathodes Having Two Crystallographic Structures: Fd$\bar{3}$m and P 4332. *Chem. Mater.* **2004**, *16*, 906−914.

(6) Manthiram, A.; Chemelewski, K.; Lee, E.-S. A Perspective on the High-Voltage LiMn1.5Ni0.5O4 Spinel Cathode for Lithium-Ion Batteries. *Energy Environ. Sci.* **2014**, *7*, 1339.

(7) Cai, L.; Liu, Z.; An, K.; Liang, C. Unraveling Structural Evolution of LiNi0.5Mn1.5O4 by in Situ Neutron Diffraction. *J. Mater. Chem. A* **2013**, *1*, 6908.

(8) Kunduraci, M.; Amatucci, G. G. Synthesis and Characterization of Nanostructured 4.7 V LixMn1.5Ni0.5O4 Spinels for High-Power Lithium-Ion Batteries. *J. Electrochem. Soc.* **2006**, *153*, A1345.

(9) Zheng, J.; Xiao, J.; Yu, X.; Kovarik, L.; Gu, M.; Omenya, F.; Chen, X.; Yang, X.-Q.; Liu, J.; Graff, G. L.; Whittingham, M. S.; Zhang, J.-G. Enhanced Li+ Ion Transport in LiNi0.5Mn1.5O4 through Control of Site Disorder. *Phys. Chem. Chem. Phys.* **2012**, *14*, 13515.

(10) Kunduraci, M.; Amatucci, G. G. Effect of Oxygen Non-Stoichiometry and Temperature on Cation Ordering in LiMn2-XNixO4 Spinels. *J. Power Sources* **2007**, *165*, 359−367.

(11) Pasero, D.; Reeves, N.; Pralong, V.; West, A. R. Oxygen Nonstoichiometry and Phase Transitions in LiMn 1.5Ni0.5O4−δ. *J. Electrochem. Soc.* **2008**, *155*, A282.

(12) Cabana, J.; Casas-Cabanas, M.; Omenya, F. O.; Chernova, N. A.; Zeng, D.; Whittingham, M. S.; Grey, C. P. Composition-Structure Relationships in the Li-Ion Battery Electrode Material LiNi 0.5 Mn 1.5 O 4. *Chem. Mater.* **2012**, *24*, 2952−2964.

(13) Kunduraci, M.; Al-Sharab, J. F.; Amatucci, G. G. High-Power Nanostructured LiMn2-XNixO4 High-Voltage Lithium-Ion Battery Electrode Materials. *Chem. Mater* **2006**, *18*, 3585−3592.

(14) Yoon, J.; Kim, D.; Um, J. H.; Jeong, M.; Oh, W.; Yoon, W.-S. Effect of Local Structural Changes on Rate Capability of LiNi 0.5 Mn 1.5 O 4−δ Cathode Material for Lithium Ion Batteries. *J. Alloys Compd.* **2016**, *686*, 593−600.

(15) Amin, R.; Belharouk, I. Part I: Electronic and Ionic Transport Properties of the Ordered and Disordered LiNi 0.5 Mn 1.5 O 4 Spinel Cathode. *J. Power Sources* **2017**, *348*, 311−317.

(16) Moorhead-Rosenberg, Z.; Huq, A.; Goodenough, J. B.; Manthiram, A. Electronic and Electrochemical Properties of Li 1− x Mn 1.5 Ni 0.5 O 4 Spinel Cathodes As a Function of Lithium Content and Cation Ordering. *Chem. Mater.* **2015**, *27*, 6934−6945.

(17) Duncan, H.; Hai, B.; Leskes, M.; Grey, C. P.; Chen, G. Relationships between Mn 3+ Content, Structural Ordering, Phase Transformation, and Kinetic Properties in LiNi x Mn 2− x O 4 Cathode Materials. *Chem. Mater.* **2014**, *26*, 5374−5382.

(18) Samarasingha, P. B.; Sottmann, J.; Margadonna, S.; Emerich, H.; Nilsen, O.; Fjellvåg, H. In Situ Synchrotron Study of Ordered and Disordered LiMn 1.5 Ni 0.5 O 4 as Lithium Ion Battery Positive Electrode. *Acta Mater.* **2016**, *116*, 290−297.

(19) Lee, E.; Persson, K. A. Solid-Solution Li Intercalation as a Function of Cation Order/Disorder in the High-Voltage LixNi0.5Mn1.5O4 Spinel. *Chem. Mater.* **2013**, *25*, 2885−2889.

(20) Casas-Cabanas, M.; Kim, C.; Rodríguez-Carvajal, J.; Cabana, J. Atomic Defects during Ordering Transitions in LiNi $_{0.5}$ Mn $_{1.5}$ O $_{4}$ and Their Relationship with Electrochemical Properties. *J. Mater. Chem. A* **2016**, *4*, 8255−8262.

(21) Lin, M.; Ben, L.; Sun, Y.; Wang, H.; Yang, Z.; Gu, L.; Yu, X.; Yang, X.-Q.; Zhao, H.; Yu, R.; Armand, M.; Huang, X. Insight into the Atomic Structure of High-Voltage Spinel LiNi 0.5 Mn 1.5 O 4 Cathode Material in the First Cycle. *Chem. Mater.* **2015**, *27*, 292−303.

(22) Tang, D.; Sun, Y.; Yang, Z.; Ben, L.; Gu, L.; Huang, X. Surface Structure Evolution of LiMn $_{2}$ O $_{4}$ Cathode Material upon Charge/Discharge. *Chem. Mater.* **2014**, *26*, 3535−3543.

(23) Aktekin, B.; Valvo, M.; Smith, R. I.; Sørby, M. H.; Lodi Marzano, F.; Zipprich, W.; Brandell, D.; Edström, K.; Brant, W. R. Cation Ordering and Oxygen Release in LiNi 0.5− x Mn 1.5+ x O 4−

y (LNMO): In Situ Neutron Diffraction and Performance in Li Ion Full Cells. *ACS Appl. Energy Mater.* **2019**, *2*, 3323−3335.
(24) Ben, L.; Yu, H.; Chen, B.; Chen, Y.; Gong, Y.; Yang, X.; Gu, L.; Huang, X. Unusual Spinel-to-Layered Transformation in LiMn2O4-Cathode Explained by Electrochemical and Thermal Stability Investigation. *ACS Appl. Mater. Interfaces* **2017**, *9*, 35463−35475.
(25) Massel, F. *Anion Redox Processes in Novel Battery Cathode Materials Investigated by Soft X-Ray Spectroscopy*; Acta Universitatis Upsaliensis, 2019.
(26) Mizokawa, T.; Wakisaka, Y.; Sudayama, T.; Iwai, C.; Miyoshi, K.; Takeuchi, J.; Wadati, H.; Hawthorn, D. G.; Regier, T. Z.; Sawatzky, G. A. Role of Oxygen Holes in LixCoO2 Revealed by Soft X-Ray Spectroscopy. *Phys. Rev. Lett.* **2013**, *111*, No. 056404.
(27) Liu, H.; Wang, J.; Zhang, X.; Zhou, D.; Qi, X.; Qiu, B.; Fang, J.; Kloepsch, R.; Schumacher, G.; Liu, Z.; Li, J. Morphological Evolution of High-Voltage Spinel LiNi 0.5 Mn 1.5 O 4 Cathode Materials for Lithium-Ion Batteries: The Critical Effects of Surface Orientations and Particle Size. *ACS Appl. Mater. Interfaces* **2016**, *8*, 4661−4675.
(28) Stöhr, J. *NEXAFS Spectroscopy*; Springer Series in Surface Sciences; Springer Berlin Heidelberg: Berlin, Heidelberg, 1992; Vol. *25*.
(29) Aktekin, B.; Younesi, R.; Zipprich, W.; Tengstedt, C.; Brandell, D.; Edström, K. The Effect of the Fluoroethylene Carbonate Additive in LiNi 0.5 Mn 1.5 O 4 - Li 4 Ti 5 O 12 Lithium-Ion Cells. *J. Electrochem. Soc.* **2017**, *164*, A942−A948.
(30) Lindgren, F.; Rehnlund, D.; Källquist, I.; Nyholm, L.; Edström, K.; Hahlin, M.; Maibach, J. Breaking Down a Complex System: Interpreting PES Peak Positions for Cycled Li-Ion Battery Electrodes. *J. Phys. Chem. C* **2017**, No. 27303.
(31) Chen, Y.; Cheng, Y.; Li, J.; Feygenson, M.; Heller, W. T.; Liang, C.; An, K. Lattice-Cell Orientation Disorder in Complex Spinel Oxides. *Adv. Energy Mater.* **2017**, *7*, No. 1601950.
(32) Kim, J. H.; Huq, A.; Chi, M.; Pieczonka, N. P. W.; Lee, E.; Bridges, C. A.; Tessema, M. M.; Manthiram, A.; Persson, K. A.; Powell, B. R. Integrated Nano-Domains of Disordered and Ordered Spinel Phases in LiNi0.5Mn1.5O4 for Li-Ion Batteries. *Chem. Mater.* **2014**, *26*, 4377−4386.
(33) Sushko, P. V.; Rosso, K. M.; Zhang, J. G.; Liu, J.; Sushko, M. L. Oxygen Vacancies and Ordering of D-Levels Control Voltage Suppression in Oxide Cathodes: The Case of Spinel LiNi0.5Mn1.5O 4-δ. *Adv. Funct. Mater.* **2013**, *23*, 5530−5535.
(34) Chen, Y.; Sun, Y.; Huang, X. Origin of the Ni/Mn Ordering in High-Voltage Spinel LiNi 0.5 Mn 1.5 O 4: The Role of Oxygen Vacancies and Cation Doping. *Comput. Mater. Sci.* **2016**, *115*, 109−116.
(35) Amdouni, N.; Zaghib, K.; Gendron, F.; Mauger, A.; Julien, C. M. Magnetic Properties of LiNi0.5Mn1.5O4spinels Prepared by Wet Chemical Methods. *J. Magn. Magn. Mater.* **2007**, *309*, 100−105.
(36) Dokko, K.; Mohamedi, M.; Anzue, N.; Itoh, T.; Uchida, I. In Situ Raman Spectroscopic Studies of LiNi $_x$ Mn $_{2-x}$ O $_4$ Thin Film Cathode Materials for Lithium Ion Secondary Batteries. *J. Mater. Chem.* **2002**, *12*, 3688−3693.
(37) Song, J.; Shin, D. W.; Lu, Y.; Amos, C. D.; Manthiram, A.; Goodenough, J. B. Role of Oxygen Vacancies on the Performance of LiNi0.5-XMn 1.5+xO 4 (x = 0, 0.05, and 0.08) Spinel Cathodes for Lithium-Ion Batteries. *Chem. Mater.* **2012**, *24*, 3101−3109.
(38) Wang, L.; Li, H.; Huang, X.; Baudrin, E. A Comparative Study of Fd-3m and P4332 "LiNi0.5Mn1.5O4". *Solid State Ionics* **2011**, *193*, 32−38.
(39) Zheng, J.; Xiao, J.; Nie, Z.; Zhang, J. Lattice Mn3+ Behaviors in Li4Ti5O12/LiNi0.5Mn1.5O4 Full Cells. *J. Power Sources* **2013**, *160*, 1264−1268.
(40) Lee, E.; Persson, K. A. Revealing the Coupled Cation Interactions behind the Electrochemical Profile of LixNi0.5Mn1.5O4. *Energy Environ. Sci.* **2012**, *5*, 6047.
(41) Lau, L. W. M.; Gerson, A. R.; Payne, B. P.; Smart, R. S. C.; Biesinger, M. C.; Grosvenor, A. P. Resolving Surface Chemical States in XPS Analysis of First Row Transition Metals, Oxides and Hydroxides: Cr, Mn, Fe, Co and Ni. *Appl. Surf. Sci.* **2011**, *257*, 2717−2730.
(42) Assat, G.; Foix, D.; Delacourt, C.; Iadecola, A.; Dedryvère, R.; Tarascon, J. M. Fundamental Interplay between Anionic/Cationic Redox Governing the Kinetics and Thermodynamics of Lithium-Rich Cathodes. *Nat. Commun.* **2017**, *8*, No. 2219.
(43) Fu, Z.; Hu, J.; Hu, W.; Yang, S.; Luo, Y. Quantitative Analysis of Ni 2+ /Ni 3+ in Li[Ni x Mn y Co z]O 2 Cathode Materials: Non-Linear Least-Squares Fitting of XPS Spectra. *Appl. Surf. Sci.* **2018**, *441*, 1048−1056.
(44) Grosvenor, A. P.; Biesinger, M. C.; Smart, R. S. C.; McIntyre, N. S. New Interpretations of XPS Spectra of Nickel Metal and Oxides. *Surf. Sci.* **2006**, *600*, 1771−1779.
(45) Van Veenendaal, M. A.; Sawatzky, G. A. Nonlocal Screening Effects in 2p X-Ray Photoemission Spectroscopy Core-Level Line Shapes of Transition Metal Compounds. *Phys. Rev. Lett.* **1993**, *70*, 2459−2462.
(46) Atanasov, M.; Reinen, D. Non-Local Electronic Effects in Core-Level Photoemission, UV and Optical Electronic Absorption Spectra of Nickel Oxides. *J. Electron Spectrosc. Relat. Phenom.* **1997**, *86*, 185−199.
(47) Qiao, R.; Chin, T.; Harris, S. J.; Yan, S.; Yang, W. Spectroscopic Fingerprints of Valence and Spin States in Manganese Oxides and Fluorides. *Curr. Appl. Phys.* **2013**, *13*, 544−548.
(48) Mukerjee, S.; Yang, X. Q.; Sun, X.; Lee, S. J.; McBreen, J.; Ein-Eli, Y. In Situ Synchrotron X-Ray Studies on Copper-Nickel 5 V Mn Oxide Spinel Cathodes for Li-Ion Batteries. *Electrochim. Acta* **2004**, *49*, 3373−3382.
(49) Qiao, R.; Wray, L. A.; Kim, J.-H.; Pieczonka, N. P. W.; Harris, S. J.; Yang, W. Direct Experimental Probe of the Ni(II)/Ni(III)/Ni(IV) Redox Evolution in LiNi 0.5 Mn 1.5 O 4 Electrodes. *J. Phys. Chem. C* **2015**, *119*, 27228−27233.
(50) Wang, H.; Ge, P.; Riordan, C. G.; Brooker, S.; Woomer, C. G.; Collins, T.; Melendres, C. A.; Graudejus, O.; Bartlett, N.; Cramer, S. P. Integrated X-Ray L Absorption Spectra. Counting Holes in Ni Complexes. *J. Phys. Chem. B* **1998**, *102*, 8343−8346.
(51) Matsubara, M.; Uozumi, T.; Kotani, A.; Parlebas, J. C. Charge Transfer Excitation in Resonant X-Ray Emission Spectroscopy of NiO. *J. Phys. Soc. Jpn.* **2005**, *74*, 2052−2060.
(52) Lu, Y.; Betto, D.; Fürsich, K.; Suzuki, H.; Kim, H. H.; Cristiani, G.; Logvenov, G.; Brookes, N. B.; Benckiser, E.; Haverkort, M. W.; Khaliullin, G.; Le Tacon, M.; Minola, M.; Keimer, B. Site-Selective Probe of Magnetic Excitations in Rare-Earth Nickelates Using Resonant Inelastic X-Ray Scattering. *Phys. Rev. X* **2018**, *8*, No. 031014.
(53) Giordano, L.; Karayaylali, P.; Yu, Y.; Katayama, Y.; Maglia, F.; Lux, S.; Shao-Horn, Y. Chemical Reactivity Descriptor for the Oxide-Electrolyte Interface in Li-Ion Batteries. *J. Phys. Chem. Lett.* **2017**, *8*, 3881−3887.
(54) Saubanère, M.; McCalla, E.; Tarascon, J. M.; Doublet, M. L. The Intriguing Question of Anionic Redox in High-Energy Density Cathodes for Li-Ion Batteries. *Energy Environ. Sci.* **2016**, *9*, 984−991.
(55) Freiberg, A. T. S.; Roos, M. K.; Wandt, J.; De Vivie-Riedle, R.; Gasteiger, H. A. Singlet Oxygen Reactivity with Carbonate Solvents Used for Li-Ion Battery Electrolytes. *J. Phys. Chem. A* **2018**, *122*, 8828−8839.
(56) Leanza, D.; Mirolo, M.; Vaz, C. A. F.; Novak, P.; El Kazzi, M. Surface Degradation and Chemical Electrolyte Oxidation Induced by the Oxygen Released from Layered Oxide Cathodes in Li-Ion Batteries. *Batteries Supercaps* **2019**, *2*, 482−492.
(57) Jarry, A.; Gottis, S.; Yu, Y.-S.; Roque-Rosell, J.; Kim, C.; Cabana, J.; Kerr, J.; Kostecki, R. The Formation Mechanism of Fluorescent Metal Complexes at the Li x Ni 0.5 Mn 1.5 O 4−δ /Carbonate Ester Electrolyte Interface. *J. Am. Chem. Soc.* **2015**, *137*, 3533−3539.
(58) Jung, R.; Metzger, M.; Maglia, F.; Stinner, C.; Gasteiger, H. A. Oxygen Release and Its Effect on the Cycling Stability of LiNi$_x$ Mn$_y$ Co$_z$ O$_2$ (NMC) Cathode Materials for Li-Ion Batteries. *J. Electrochem. Soc.* **2017**, *164*, A1361−A1377.

https://dx.doi.org/10.1021/acsaem.0c01075
ACS Appl. Energy Mater. 2020, 3, 6001−6013

(59) Liu, Y.-S.; Pickup, D. M.; Chadwick, A. V.; Roberts, M. R.; Bruce, P. G.; Edström, K.; Hao, R.; Guerrini, N.; Duda, L. C.; Luo, K.; Guo, J. Charge-Compensation in 3d-Transition-Metal-Oxide Intercalation Cathodes through the Generation of Localized Electron Holes on Oxygen. *Nat. Chem.* **2016**, *8*, 684−691.

https://dx.doi.org/10.1021/acsaem.0c01075
ACS Appl. Energy Mater. 2020, 3, 6001−6013